JURNAL MATEMATIKA, STATISTIKA DAN KOMPUTASI e-ISSN: 2614-8811
Published by Departement of Mathematics, Hasanuddin University, Indonesia
https://journal.unhas.ac.id/index.php/jmsk/index
Vol. 22, No. 2, January 2026, pp. 407-416
DOI: 10.20956/j.v22i2.47866

Numerical Simulation of Thermal Newtonian Fluid Flow Driven by Horizontal Convection in A Porous Cavity

Rina Reorita[1], Agus Yodi Gunawan[2]*, Novry Erwina[3]
[1] *Doctoral Program of Mathematics, Faculty of Mathematics and Natural Sciences, Institut Teknologi Bandung*
[2,3] *Department of Mathematics, Faculty of Mathematics and Natural Sciences, Institut Teknologi Bandung*
***Email**: [1]30122002@mahasiswa.itb.ac.id; [2*]ayodi@itb.ac.id; [3]nerwina@math.itb.ac.id*
[*] *Corresponding author*

Abstract

Horizontal convection is a distinct form of natural convection where flow is generated by uneven buoyancy along a horizontal boundary. This study presents a numerical simulation of horizontal convection within a porous rectangular cavity. The flow is driven by a non-uniform heating on the top surface, while the other boundaries are thermally insulated. We derive a governing equation involving four dimensionless parameters: the Darcy number, the Rayleigh number, the viscosity ratio, and the geometric aspect ratio. This equation is solved numerically through the finite difference method. Our investigation emphasizes how the Rayleigh number and viscosity ratio influence the flow of the thermal fluid. The results show that viscosity inhibits convection, thereby weakening the thermal boundary layer.

Keywords: heat transfer; porous medium; non-uniform heating; finite-difference.

1. INTRODUCTION

Convection is the transfer of thermal energy through the movement of fluids, like liquids or gases, driven by temperature differences. In this process, the hotter fluid becomes less dense and rises, pushing the cooler fluid aside. Understanding the convection process is crucial because it has many practical uses. For instance, it plays a role in building ventilation, cooling systems in nuclear reactors [21], solar collectors [15], lubrication, and food processing [10].

From a geometric perspective, the study of convection primarily involves analyzing fluid flow and heat transfer within a domain. Many researchers simplify the complexity of real-world domains by modeling them as rectangular cavities. To study convection in a rectangular cavity, three main models can be employed: Rayleigh-Bénard convection, vertical convection, and horizontal convection [20]. Rayleigh-Bénard convection is a classic form of fluid convection and a common topic for many researchers. Rayleigh-Bénard convection occurs when a fluid is heated from below and cooled from above [22]. In Rayleigh-Bénard convection, a vertical temperature gradient causes circulation cells due to thermal instability, which is essential for studying thermal fluid dynamics

and heat transfer in the oceans, atmosphere, and Earth's crust [5]. Vertical convection occurs when the main temperature difference is vertical, regardless of the boundary's orientation, and is commonly seen in vertical pipes and heat exchangers. It involves heating one vertical wall while cooling the opposite [17]. Horizontal convection is a unique form of natural convection where the flow is caused by uneven buoyancy along a horizontal boundary [7]. Horizontal convection occurs in natural settings such as oceanic circulations [8], shallow seas, solar ponds, and horizontal thermal reservoirs.

Research on horizontal convection is less common than on Rayleigh-Bénard convection. It is challenging to study experimentally because maintaining a steady temperature gradient in a laboratory setting is difficult. Several researchers, including Yan et al. [18], Noto et al. [11-12], and Yan and He [19], contributed to this field. Additionally, analyzing horizontal convection is more complex both mathematically and physically, especially at high Rayleigh numbers, where the circulation becomes asymmetric. Yang et al. [20] observed that fluctuating velocities increase with higher Rayleigh numbers, driven by the non-uniform temperature profile that drives fluid flow. Applying a non-uniform temperature to the top wall also prevents the fluid from sustaining deep vertical stratification [9], [16]. Even in studies by Chiu-Webster et al. [3], Sheard and King [13], and Shiskina et al. [14], the importance of large Rayleigh numbers in scaling issues was highlighted.

The complexity of horizontal convection increases when fluid moves through a porous medium, which is a material characterized by void spaces or pores [1]. The mathematical model describing convection in a porous medium is derived from Darcy's law [4], [2], where the velocity is proportional to the pressure gradient. Friction within the medium impedes fluid flow through the solid matrix. Daniels and Punpocha [4] noted that convection becomes dominant—leading to the formation of a thermal boundary layer—when the Darcy-Rayleigh number is high. However, the governing equation stated by Daniels and Punpocha [4] was limited to ideal fluids.

An ideal fluid is incompressible and has zero viscosity. It is a theoretical concept used to simplify modeling and calculations. There are no real examples of ideal fluids, but water and air are often treated as approximations.

In the present work, we study horizontal convection of a Newtonian fluid in a porous rectangular cavity. A Newtonian fluid is one where shear stress is directly proportional to shear rate at a constant temperature and pressure, defined by a constant dynamic viscosity. In this research, we highlight the impact of viscosity on flow behavior, as reflected in a friction term in the governing equation. We solve the governing equation numerically using the finite difference method. The findings of this research can contribute to the development of thermal management systems and energy-efficient materials where viscous resistance is a key factor.

This paper is structured into five sections. Following this introduction, Section 2 details the mathematical formulation of the problem along with the boundary conditions. It also covers nondimensional parameters and scaling arguments. Section 3 explains the numerical procedure, including stability, convergence considerations, and grid refinement test. The results and physical interpretations are discussed in Section 4, while Section 5 summarizes the key conclusions.

2. MATHEMATICAL FORMULATION

2.1 The model

A schematic diagram of the problem is shown in Figure 2.1. Consider a fluid confined within a domain $\{0 \le x \le \ell_x, 0 \le y \le \ell_y\}$ saturated with a porous medium. A non-uniform temperature,

$$T_* = T_{0_*} + \Delta T_* S\left(\frac{x_*}{\ell_x}\right),$$

is applied to the top surface, while the side and bottom walls are thermally insulated. The T_{0_*} denotes a reference temperature and ΔT_* indicates the temperature difference on the surface. As proposed by Daniels and Punpocha [4], the $S\left(\frac{x_*}{\ell_x}\right)$ function represents a monotonic function that has a value of 0 at $x_* = 0$ and 1 at $x_* = \ell_x$.

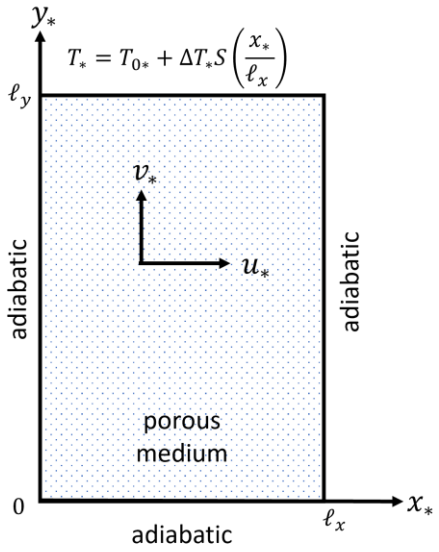

Figure 2.1. A schematic diagram of the system

Assuming the walls of the cavity are impermeable and the porous medium inside the system is homogeneous and isotropic, we can write the steady-state governing equation that satisfies the Darcy law as follows:

$$\frac{\partial u_*}{\partial x_*} + \frac{\partial v_*}{\partial y_*} = 0, \tag{2.1}$$

$$\frac{\mu}{K} u_* = -\frac{\partial p_*}{\partial x_*} + \mu_p \left(\frac{\partial^2 u_*}{\partial {x_*}^2} + \frac{\partial^2 u_*}{\partial {y_*}^2}\right), \tag{2.2}$$

$$\frac{\mu}{K} v_* = -\frac{\partial p_*}{\partial y_*} + \mu_p \left(\frac{\partial^2 v_*}{\partial {x_*}^2} + \frac{\partial^2 v_*}{\partial {y_*}^2}\right) - \rho g, \tag{2.3}$$

$$u_* \frac{\partial T_*}{\partial x_*} + v_* \frac{\partial T_*}{\partial y_*} = \alpha \left(\frac{\partial^2 T_*}{\partial {x_*}^2} + \frac{\partial^2 T_*}{\partial {y_*}^2}\right), \tag{2.4}$$

where u_* and v_* are the velocity components in the x_* and y_* directions, respectively, p_* is the pressure, ρ is the fluid density, and T_* is the fluid temperature. The parameter μ is the absolute viscosity, and μ_p is the effective viscosity of the fluid. These viscosity parameters are assumed to be independent of temperature. If $\mu = \mu_p$, then we derive the Brinkman-Darcy equation. The symbol K is the permeability of the porous medium, g is the gravitational acceleration, and α is the thermal diffusivity.

The temperature at the top boundary drives the fluid, inducing variations in the density of the fluid molecules. The Boussinesq approximation assumes that the variation in fluid density is directly

proportional to the temperature. By applying the Boussinesq approximation and the cross-differentiation of Equations (2.2) and (2.3), we can write the governing equation as follows:

$$\frac{\partial u_*}{\partial x_*}+\frac{\partial v_*}{\partial y_*}=0, \tag{2.5}$$

$$\frac{\mu}{K}\left(\frac{\partial v_*}{\partial x_*}-\frac{\partial u_*}{\partial y_*}\right)=\mu_p\left(\frac{\partial^3 v_*}{\partial {x_*}^3}+\frac{\partial^3 v_*}{\partial x_* \partial {y_*}^2}-\frac{\partial^3 u_*}{\partial {x_*}^2 \partial y_*}-\frac{\partial^3 u_*}{\partial {y_*}^3}\right)+\rho_0 g\beta\frac{\partial(T_*-T_{0*})}{\partial x_*}, \tag{2.6}$$

$$u_*\frac{\partial T_*}{\partial x_*}+v_*\frac{\partial T_*}{\partial y_*}=\alpha\left(\frac{\partial^2 T_*}{\partial {x_*}^2}+\frac{\partial^2 T_*}{\partial {y_*}^2}\right), \tag{2.7}$$

where ρ_0 is the density reference and β is the thermal expansion coefficient.

Next, we define a stream function $\psi(x,y)$ that satisfies the continuity equation (2.5) in the following manner:

$$u_*=\frac{\partial \psi_*}{\partial y_*}, \qquad v_*=-\frac{\partial \psi_*}{\partial x_*}. \tag{2.8}$$

The stream function illustrates the trajectories of particles, which can be used to draw the streamlines. Applying Equation (2.8) to Equation (2.5) – (2.7), we derive the governing equation in the stream functions-energy formulation as follows:

$$\frac{\mu}{K}\left(\frac{\partial^2 \psi_*}{\partial {x_*}^2}+\frac{\partial^2 \psi_*}{\partial {y_*}^2}\right)=-\rho_0 g\beta\frac{\partial(T_*-T_0)}{\partial x_*}+\mu_p\left(\frac{\partial^4 \psi_*}{\partial {x_*}^4}+2\frac{\partial^4 \psi_*}{\partial {x_*}^2\partial {y_*}^2}+\frac{\partial^4 \psi_*}{\partial {y_*}^4}\right), \tag{2.9}$$

$$\frac{\partial \psi_*}{\partial y_*}\frac{\partial T_*}{\partial x_*}-\frac{\partial \psi_*}{\partial x_*}\frac{\partial T_*}{\partial y_*}=\alpha\left(\frac{\partial^2 T_*}{\partial {x_*}^2}+\frac{\partial^2 T_*}{\partial {y_*}^2}\right). \tag{2.10}$$

2.2 Dimensionless governing equation

For clarity and to generalize the analysis, the governing equations (2.9) – (2.10) are transformed into dimensionless form using the following dimensionless quantities:

$$x=\frac{x_*}{\ell_y}, \qquad y=\frac{y_*}{\ell_y}, \qquad \psi=\frac{1}{\alpha}\psi_*, \qquad T=\frac{T_*-T_{0*}}{\Delta T_*},$$

$$R_a=\frac{\rho_0 g\beta\Delta T {\ell_y}^3}{\mu\alpha}, \qquad \tilde{\mu}=\frac{\mu_p}{\mu}, \qquad D_a=\frac{K}{{\ell_y}^2}, \qquad A=\frac{\ell_x}{\ell_y}.$$

Then, the dimensionless governing equations can be written as follows:

$$\frac{1}{D_a}\left(\frac{\partial^2 \psi}{\partial x^2}+\frac{\partial^2 \psi}{\partial y^2}\right)=-R_a\frac{\partial T}{\partial x}+\tilde{\mu}\left(\frac{\partial^4 \psi}{\partial x^4}+2\frac{\partial^4 \psi}{\partial x^2\partial y^2}+\frac{\partial^4 \psi}{\partial y^4}\right), \tag{2.11}$$

$$\frac{\partial \psi}{\partial y}\frac{\partial T}{\partial x}-\frac{\partial \psi}{\partial x}\frac{\partial T}{\partial y}=\frac{\partial^2 T}{\partial x^2}+\frac{\partial^2 T}{\partial y^2}, \tag{2.12}$$

with the boundary conditions:

$$\psi=0, \qquad \frac{\partial T}{\partial x}=0, \text{ on } x=0, A, \tag{2.13}$$

$$\psi = 0, \quad \frac{\partial T}{\partial y} = 0, \text{ on } y = 0, \tag{2.14}$$

$$\psi = 0, \quad T = S\left(\frac{x}{A}\right). \text{ on } y = 1. \tag{2.15}$$

Now, we identify four dimensionless parameters: the Rayleigh number R_a, the Darcy number D_a, the viscosity ratio $\tilde{\mu}$, and the geometric aspect ratio A. We solve the Equations (2.11) – (2.12) with boundary conditions (2.13) – (2.15) numerically, as described in the following section.

3. SOLUTION PROCEDURE

Currently, we are working with a steady state system (2.11) – (2.12). To find the steady-state solution, a time marching method is used. In this method, artificial time-derivative terms are added to the steady-state equations, enabling the solution to progress in a simulated time until a steady condition is achieved. This approach improves numerical stability and convergence, especially for strongly coupled nonlinear systems.

We introduce artificial time derivatives on the left-hand side of the governing equations (2.11) and (2.12), as written as follows:

$$\frac{\partial \psi}{\partial t} = \frac{1}{D_a}\left(\frac{\partial^2 \psi}{\partial x^2} + \frac{\partial^2 \psi}{\partial y^2}\right) + R_a \frac{\partial T}{\partial x} - \tilde{\mu}\left(\frac{\partial^4 \psi}{\partial x^4} + 2\frac{\partial^4 \psi}{\partial x^2 \partial y^2} + \frac{\partial^4 \psi}{\partial y^4}\right), \tag{3.1}$$

$$\frac{\partial T}{\partial t} = \frac{\partial^2 T}{\partial x^2} + \frac{\partial^2 T}{\partial y^2} - \frac{\partial \psi}{\partial y}\frac{\partial T}{\partial x} + \frac{\partial \psi}{\partial x}\frac{\partial T}{\partial y}, \tag{3.2}$$

and derive the steady-state solution in the limit of large time.

Equations (3.1) and (3.2) are then discretized using the finite difference method, employing a forward difference for the temporal variable and second-order accurate central differences for the spatial variables. The discrete form of Equations (3.1) and (3.2) is written as follows:

$$\begin{aligned}
\psi_{i,j}^{n+1} = \psi_{i,j}^{n} &+ \frac{1}{D_a}\frac{\Delta t}{(\Delta x)^2}\left[\psi_{i+1,j}^{n} - 2\psi_{i,j}^{n} + \psi_{i-1,j}^{n}\right] + \frac{1}{D_a}\frac{\Delta t}{(\Delta y)^2}\left[\psi_{i,j+1}^{n} - 2\psi_{i,j}^{n} + \psi_{i,j-1}^{n}\right] \\
&+ R_a \frac{\Delta t}{2\Delta x}\left[T_{i+1,j}^{n} - T_{i-1,j}^{n}\right] \\
&- \tilde{\mu}\frac{\Delta t}{(\Delta x)^4}\left[\psi_{i-2,j}^{n} - 4\psi_{i-1,j}^{n} + 6\psi_{i,j}^{n} - 4\psi_{i+1,j}^{n} + \psi_{i,+2j}^{n}\right] \\
&- 2\tilde{\mu}\frac{\Delta t}{(\Delta x)^2(\Delta y)^2}\left[\psi_{i-1,j-1}^{n} - 2\psi_{i-1,j}^{n} + \psi_{i-1,j+1}^{n} - 2\psi_{i,j-1}^{n} + 4\psi_{i,j}^{n}\right. \\
&\left. - 2\psi_{i,j+1}^{n} + \psi_{i+1,j-1}^{n} - 2\psi_{i+1,j}^{n} + \psi_{i+1,j+1}^{n}\right] \\
&- \tilde{\mu}\frac{\Delta t}{(\Delta y)^4}\left[\psi_{i,j-2}^{n} - 4\psi_{i,j-1}^{n} + 6\psi_{i,j}^{n} - 4\psi_{i,j+1}^{n} + \psi_{i,j+2}^{n}\right],
\end{aligned} \tag{3.3}$$

$$\begin{aligned}
T_{i,j}^{n+1} = T_{i,j}^{n} &+ \frac{\Delta t}{(\Delta x)^2}\left[T_{i+1,j}^{n} - 2T_{i,j}^{n} + T_{i-1,j}^{n}\right] + \frac{\Delta t}{(\Delta y)^2}\left[T_{i,j+1}^{n} - 2T_{i,j}^{n} + T_{i,j-1}^{n}\right] \\
&- \frac{1}{4}\frac{\Delta t}{\Delta x \Delta y}\left[\psi_{i,j+1}^{n} - \psi_{i,j-1}^{n}\right]\left[T_{i+1,j}^{n} - T_{i-1,j}^{n}\right] \\
&+ \frac{1}{4}\frac{\Delta t}{\Delta x \Delta y}\left[\psi_{i+1,j}^{n} - \psi_{i-1,j}^{n}\right]\left[T_{i,j+1}^{n} - T_{i,j-1}^{n}\right].
\end{aligned} \tag{3.4}$$

The stability criterion is open for discussion, but in this study, we follow the work of Haque et al. [6] by setting Δt to satisfy the diffusion-advection stability criterion, as outlined below.

$$\Delta t \leq \frac{1}{2}\frac{\Delta x^2 \Delta y^2}{\Delta x^2 + \Delta y^2} \quad \text{and} \quad \frac{\left|\frac{\partial \psi}{\partial y}\right| \Delta t}{\Delta x} + \frac{\left|\frac{\partial \psi}{\partial x}\right| \Delta t}{\Delta y} \leq C_{max},$$

where C_{max} is the maximum Courant number.

For the initial conditions, we assume that the fluid is at rest and that heat is transferred by pure conduction from the top boundary. Following the work of Daniels and Punpocha [4], we choose the temperature profile on the top boundary as follows:

$$S\left(\frac{x}{A}\right) = \frac{1}{2}\left(1 - \cos\left(\frac{\pi x}{A}\right)\right), \qquad 0 \leq x \leq A.$$

Starting from the initial conditions, the stream function and temperature are updated until the changes in ψ and T are small enough to satisfy the convergence criterion:

$$|(\psi, T)_{new} - (\psi, T)_{old}| \leq 10^{-6}.$$

Before proceeding further, we perform a grid refinement test to evaluate the effect of grid size on the solution. We use parameters $D_a = 1, R_a = 1000$, and $\tilde{\mu} = 0.01$ to check the maximum value of the stream function ψ_{max} in various grid sizes. Afterwards, we check the relative differences of ψ_{max} by the following equation.

$$\text{Relative difference} = \frac{\left|\psi_{max,N_k} - \psi_{max,N_{k-1}}\right|}{\psi_{max,N_k}} \times 100\%, \tag{3.5}$$

where ψ_{max,N_k} is the maximum value of the stream function using the grid $N_k \times N_k$. The results are displayed in Table 3.1. From Table 3.1, we find that ψ_{max} smoothly increases, while the relative differences from 40 × 40 to 50 × 50 is slightly increased due to truncation and nonlinear error. However, our simulation reaches grid independence at around 60 × 60, because as we increase the grid size, the relative difference is less than 1%. This means that increasing the grid size beyond 60 × 60 will not significantly change ψ_{max} or other flow features. In the next section, we use this grid size to perform numerical simulations using a set of key parameters specified in Equations (3.1) and (3.2) to analyze flow behavior and heat transfer.

Table 3.1. Grid refinement test by means of the maximum stream function

Number of grids in *x*-*y*	ψ_{max}	Relative difference
30 × 30	5.4746	-
40 × 40	5.4791	0.0821
50 × 50	5.4965	0.3166
60 × 60	5.5013	0.0873
70 × 70	5.5019	0.0109

4. RESULTS

The numerical results are presented by outlining streamlines and isotherms for four key parameters: the Darcy number, the Rayleigh number, the viscosity ratio, and the geometric aspect ratio. The Darcy number reflects the permeability of the medium. The Rayleigh number measures buoyancy forces. The viscosity ratio indicates friction caused by viscous fluid, while the geometric aspect ratio indicates the shape of the cavity. To focus on emphasizing the effect of viscosity on heat transfer, we set a fixed $D_a = 1$ and $A = 1$, while R_a and $\tilde{\mu}$ are varied.

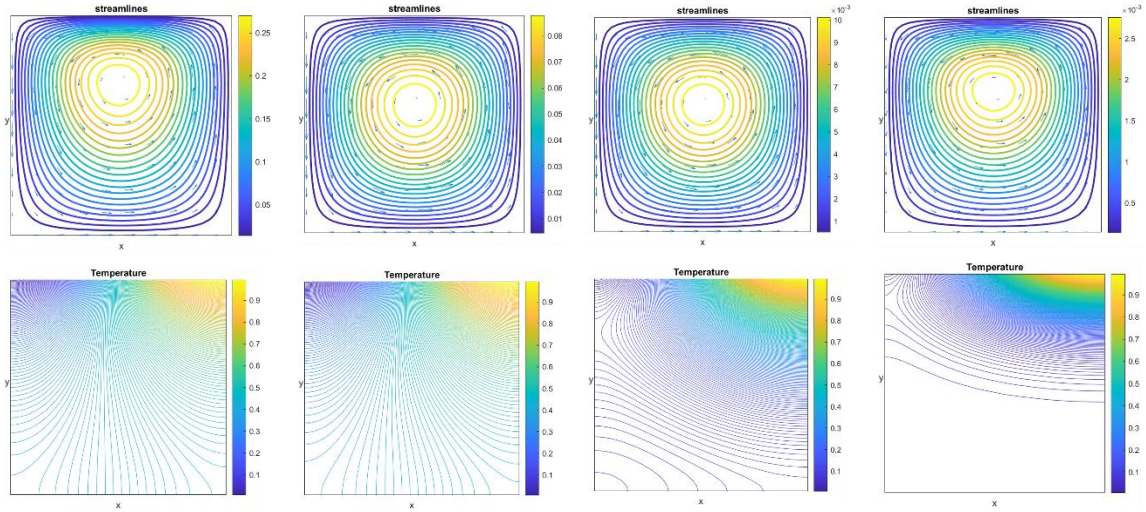

(a) $\tilde{\mu} = 0$ (b) $\tilde{\mu} = 0.1$ (c) $\tilde{\mu} = 1$ (d) $\tilde{\mu} = 1.5$

Figure 4.1. Streamlines and isotherms for $R_a = 10$

Figure 4.1 illustrates streamlines and isotherms for $R_a = 10$ at different viscosity ratios: $\tilde{\mu} = 0, 0.1, 1,$ and 1.5. A viscosity ratio of zero indicates an ideal fluid (such as water and air), which has no viscous friction. Figure 4.1(a) demonstrates how an ideal fluid can be easily driven by a small buoyancy force. The maximum streamline, $\psi_{max} = 0.27$, is located at the center of circulation. The isotherms show that heat is transferred throughout the cavity, with the contours symmetric about $x = 1/2$. When the viscosity ratio increases to $\tilde{\mu} = 0.1$, as shown in Figure 4.1(b), the maximum streamline decreases to $\psi_{max} = 0.087$. Likewise, Figures 4.1(c) and (d) reveal that the smaller ψ_{max} becomes as the viscosity ratio rises. In these figures, the isotherms are unsymmetrical. At $R_a = 10$, the viscous fluid significantly impedes heat distribution throughout the cavity, as conduction still dominates.

Figure 4.2 illustrates how temperature evolves over time until a steady state is achieved. We choose $R_a = 10$ and $\tilde{\mu} = 0.1$ to highlight the influence of viscosity with a relatively weak buoyancy force. Initially, the domain's temperature is assumed to be zero, and heat from the top wall has not yet been distributed throughout the domain. At $t = 0.001$, conduction from the heat source begins, spreading heat around the top wall (Figure 4.2(a)). Heat layers start forming at $t = 0.01$ (Figure 4.2(b)). By $t = 0.1$, heat starts diffusing throughout the domain, reaching a steady state at $t = 1.9$ (Figures 4.2(c) and (d)).

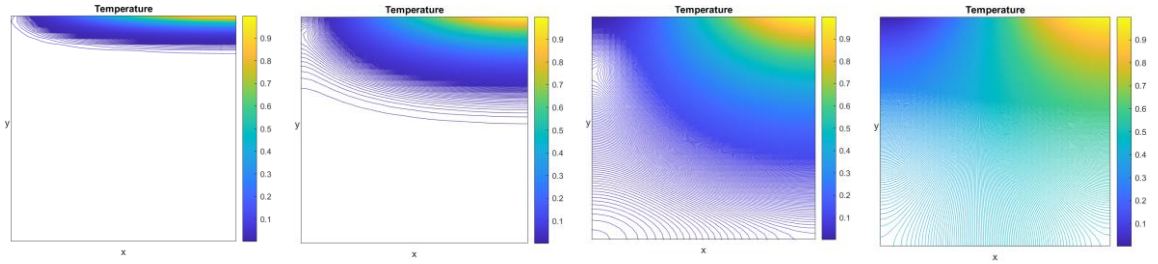

(a) $t = 0.001$ (b) $t = 0.01$ (c) $t = 0.1$ (d) $t = 1.9$

Figure 4.2. Isotherms at stages in the evolution to the steady state with $R_a = 10$ and $\tilde{\mu} = 0.1$

Next, in Figure 4.3, we apply the Rayleigh number $R_a = 1000$ at the same viscosity ratios as in Figure 4.1. Figure 4.3(a) illustrates streamlines and isotherms for an ideal fluid. With a strong buoyancy force and no viscous resistance, the circulation center shifts upward to the upper left corner, with $\psi_{max} = 6.46$. A thermal boundary layer appears near the top wall. When viscosity increases to $\tilde{\mu} = 0.1$ (Figures 4.3(b)), the circulation weakens, indicated by $\psi_{max} = 3.37$. The boundary layer diminishes even though the buoyancy force stays large. Additionally, in Figures 4.3(c) and (d), increased viscosity reduces buoyancy effects, leading streamlines to align almost horizontally.

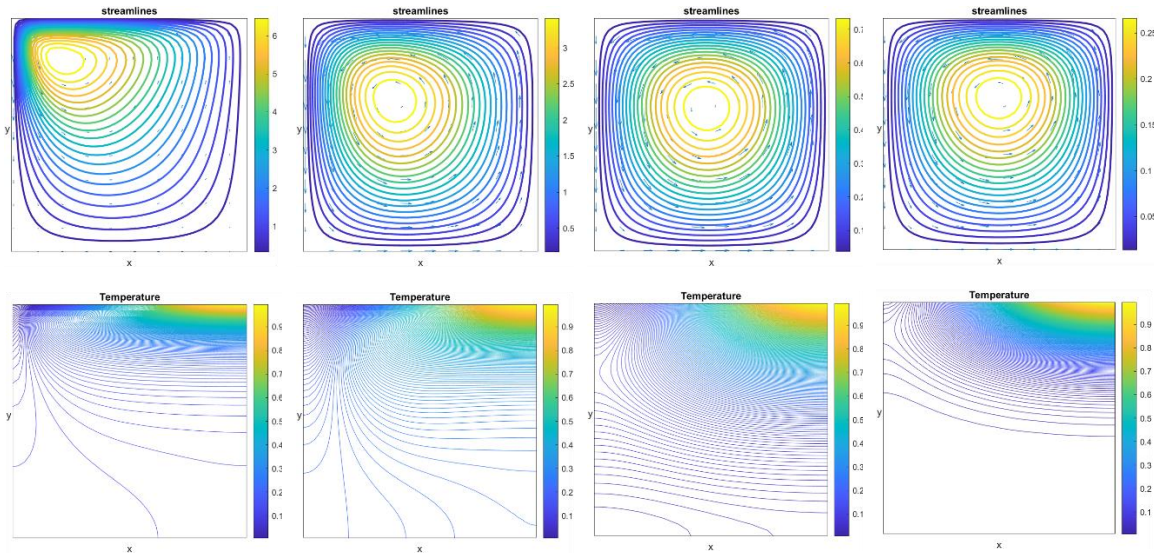

(a) $\tilde{\mu} = 0$ (b) $\tilde{\mu} = 0.1$ (c) $\tilde{\mu} = 1$ (d) $\tilde{\mu} = 1.5$

Figure 4.3. Streamlines and isotherms for $R_a = 1000$

5. CONCLUSION

In this study, we developed a mathematical model for the flow of a thermal Newtonian fluid driven by a non-uniform temperature in a porous rectangular cavity. The model includes governing equations with four main parameters: the Darcy number, Rayleigh number, viscosity ratio, and geometric aspect ratio. We solved these equations using artificial time derivatives to achieve a steady-state solution via time marching. The equations were discretized with the finite difference

method. Numerical results indicate that increasing the viscosity ratio reduces convective heat transfer.

ACKNOWLEDGEMENT

This study is part of the Penelitian Disertasi Doktor (grant number: 308/IT1.B07.1/SPP-DRI/V/2025). We would like to express our appreciation to the Ministry of Higher Education, Science, and Technology of the Republic of Indonesia for supporting this research.

CONFLICT OF INTEREST

The authors declare that there are no conflicts of interest regarding the publication of this paper.

REFERENCES

[1] Balla, C. S., Kishan, N., Gorla, R. S. R., & Gireesha, B. J., 2017. MHD boundary layer flow and heat transfer in an inclined porous square cavity filled with nanofluids. *Ain Shams Engineering Journal*, Vol. 8, No. 2, 237–254. https://doi.org/10.1016/j.asej.2016.02.010

[2] Bejan, A., 2013. *Convection Heat Transfer*, Fourth Edition. John Wiley &Sons.

[3] Chiu-Webster, S., Hinch, E. J., & Lister, J. R., 2008. Very viscous horizontal convection. In *Journal of Fluid Mechanics*, Vol. 611. https://doi.org/10.1017/S0022112008002942

[4] Daniels, P. G., & Punpocha, M., 2004. Cavity flow in a porous medium driven by differential heating. *International Journal of Heat and Mass Transfer*, Vol. 47, No. 14–16, 3017–3030. https://doi.org/10.1016/j.ijheatmasstransfer.2004.03.004

[5] Favier, B., Purseed, J., & Duchemin, L., 2019. Rayleigh-Bénard convection with a melting boundary. *Journal of Fluid Mechanics*, Vol. 858, 437–473. https://doi.org/10.1017/jfm.2018.773

[6] Haque, M. N., Akter, R., & Mojumder, M. S. H., 2025. An Efficient Explicit Scheme for Solving the 2D Heat Equation with Stability and Convergence Analysis. *Journal of Applied Mathematics and Physics*, Vol. 13, No. 07, 2234–2244. https://doi.org/10.4236/jamp.2025.137127

[7] Hossain, S., Vo, T., & Sheard, G. J., 2019. Horizontal convection in shallow enclosures scales with height, not length, at low Rayleigh numbers. *International Communications in Heat and Mass Transfer*, Vol. 109 (October). https://doi.org/10.1016/j.icheatmasstransfer.2019.104308

[8] Hossain, S., Vo, T., & Sheard, G. J., 2020. Shallow Enclosure Horizontal Convection: Insights from Asymptotic Expansion Analysis. *22nd Australasian Fluid Mechanics Conference, AFMC 2020*, *December*, 7–10. https://doi.org/10.14264/06df42f

[9] Ilicak, M., & Vallis, G. K., 2012. Simulations and scaling of horizontal convection. *Tellus, Series A: Dynamic Meteorology and Oceanography*, Vol. 64, No. 1, 1–17. https://doi.org/10.3402/tellusa.v64i0.18377

[10] Milani Shirvan, K., Mamourian, M., Mirzakhanlari, S., Rahimi, A. B., & Ellahi, R., 2017. Numerical study of surface radiation and combined natural convection heat transfer in a solar cavity receiver. *International Journal of Numerical Methods for Heat & Fluid Flow*, Vol. 27, No. 10, 2385–2399. https://doi.org/10.1108/HFF-10-2016-0419

[11] Noto, D., Terada, T., Yanagisawa, T., Miyagoshi, T., & Tasaka, Y., 2021. Developing

horizontal convection against stable temperature stratification in a rectangular container. *Physical Review Fluids*, Vol. 6, No. 8, 1–24. https://doi.org/10.1103/PhysRevFluids.6.083501

[12] Noto, D., Ulloa, H. N., Yanagisawa, T., & Tasaka, Y., 2023. Stratified horizontal convection. *Journal of Fluid Mechanics*, Vol. 970, 1–25. https://doi.org/10.1017/jfm.2023.625

[13] Sheard, G. J., & King, M. P., 2011. Horizontal convection: Effect of aspect ratio on Rayleigh number scaling and stability. *Applied Mathematical Modelling*, Vol. 35. No. 4, 1647–1655. https://doi.org/10.1016/j.apm.2010.09.041

[14] Shishkina, O., Grossmann, S., & Lohse, D., 2016. Heat and momentum transport scalings in horizontal convection. *Geophysical Research Letters*, Vol. 43, No. 3, 1219–1225. https://doi.org/10.1002/2015GL067003

[15] Singh, D. K., & Singh, S. N., 2015. Conjugate free convection with surface radiation in open top cavity. *International Journal of Heat and Mass Transfer*, Vol. 89, 444–453. https://doi.org/10.1016/j.ijheatmasstransfer.2015.05.038

[16] Tsai, T., Hussam, W. K., King, M. P., & Sheard, G. J., 2020. Transitions and scaling in horizontal convection driven by different temperature profiles. *International Journal of Thermal Sciences*, Vol. 148 (September 2019), 106166. https://doi.org/10.1016/j.ijthermalsci.2019.106166

[17] Wang, Q., Liu, H. R., Verzicco, R., Shishkina, O., & Lohse, D., 2021. Regime transitions in thermally driven high-Rayleigh number vertical convection. *Journal of Fluid Mechanics*, Vol. 917, 1–18. https://doi.org/10.1017/jfm.2021.262

[18] Yan, B., Shishkina, O., & He, X., 2021. Thermal boundary-layer structure in laminar horizontal convection. *Journal of Fluid Mechanics*, Vol. 915, 1–11. https://doi.org/10.1017/jfm.2021.226

[19] Yan, B. & He, X., 2023. Transitional fluctuations of thermal boundary layer in horizontal convection, International Journal of Heat and Mass Transfer, Vol. 200, pp. 123542, doi: 10.1016/j.ijheatmasstransfer.2022.123542

[20] Yang, T., Wang, B., Wu, J., Lu, Z., & Zhou, Q., 2021. Horizontal convection in a rectangular enclosure driven by a linear temperature profile. *Applied Mathematics and Mechanics*, Vol. 42. No. 8, 1183–1190. https://doi.org/10.1007/s10483-021-2754-5

[21] Zhou, L., Armfield, S. W., Williamson, N., Kirkpatrick, M. P., & Lin, W., 2021. Natural convection in a cavity with time-dependent flux boundary. *International Journal of Heat and Fluid Flow*, Vol. 92, 108887. https://doi.org/10.1016/j.ijheatfluidflow.2021.108887

[22] Zhu, X., Mathai, V., Stevens, R. J. A. M., Verzicco, R., & Lohse, D., 2018. Transition to the Ultimate Regime in Two-Dimensional Rayleigh-Bénard Convection. *Physical Review Letters*, Vol. 120, No. 14, 144502. https://doi.org/10.1103/PhysRevLett.120.144502